Impact of Neutron Irradiation on Mechanical Performance of FeCrAl Alloy Laser-beam Weldments

M. N. Gussev,[*] *E. Cakmak, K. G. Field*
Oak Ridge National Laboratory, P.O. Box 2008, Oak Ridge, TN 37831-6136

Abstract

Oxidation-resistant iron-chromium-aluminum (FeCrAl) alloys demonstrate better performance in Loss-of-Coolant Accidents, compared with austenitic- and zirconium-based alloys. However, further deployment of FeCrAl-based materials requires detailed characterization of their performance under irradiation; moreover, since welding is one of the key operations in fabrication of light water reactor fuel cladding, FeCrAl alloy weldment performance and properties also should be determined prior to and after irradiation. Here, advanced C35M alloy (Fe-13%Cr-5%Al) and variants with aluminum (+2%) or titanium carbide (+1%) additions were characterized after neutron irradiation in Oak Ridge National Laboratory's High Flux Isotope Reactor at 1.8–1.9 dpa in a temperature range of 195–559°C. Specimen sets included as-received (AR) materials and specimens after controlled laser-beam welding. Tensile tests with digital image correlation (DIC), scanning electron microscopy-electron back scatter diffraction analysis, fractography, and x-ray tomography analysis were performed. DIC allowed for investigating local yield stress in the weldments, deformation hardening behavior, and plastic anisotropy. Both AR and welded material revealed a high degree of radiation-induced hardening for low-temperature irradiation; however, irradiation at high-temperatures (i.e., 559°C) had little overall effect on the mechanical performance.

Keywords:

FeCrAl alloys, Laser-beam welding, Mechanical behavior, Digital image correlation, Tensile testing.

Highlights:

- Weldments of oxidation-resistant FeCrAl alloys were irradiated in a temperature range of 195–559°C to ~1.8–1.9 dpa.
- Mechanical behavior was investigated before and after irradiation for nonwelded and welded samples.
- Local yield stress (LYS) and true stress–true strain curves are presented and discussed.

---

[*] Corresponding author: gussevmn@ornl.gov

1. Introduction

Further improvements in nuclear power plant safety and performance call for materials [1,2] that can successfully withstand extreme environments, including elevated temperature, high mechanical stresses, and corrosive attack [3–6]. Additionally, acceptable price [7], radiation tolerance, and ability to survive off-normal conditions (e.g., loss-of-coolant accidents [LOCA]) [3,6] have also become important material performance metrics. Iron-chromium-aluminum (FeCrAl) alloys show promise as robust materials for use in nuclear power production applications. These alloys have shown excellent environmental compatibility [3,4,8], including compatibility with molten heavy metals [9] and high-temperature water, oxidation resistance in high-temperature air [10] and steam [6,11], and low radiation-induced swelling [12,13]. FeCrAl alloys have also been proven to be tolerant to LOCA conditions [6]. Thus, this aggregate of beneficial properties makes the FeCrAl alloy class promising for further optimization for nuclear power applications [14].

At the same time, good weldability [15], high weldment performance, and weld reparability [16] often are mandatory options for materials to be considered by the nuclear power industry. Advanced modern materials often have highly tailored microstructures and microchemistry that enhance their performance. The high-heat input from fusion-based welding leads to the localized melting of the material and inevitably the destruction or, at a minimum, degradation of the tailored microstructure and microchemistry at and near the weld. Even in regions outside the fusion zone, localized heating can be above critical temperatures (e.g., the critical temperature for recrystallization), stimulating negative changes and degradation of microstructure [17]. Welding may compromise the in-reactor performance by leading to an accelerated property degradation or switching phenomena originally suppressed by the highly tailored microstructures prior to welding and irradiation.

Thus, a critical need exists to determine the performance of irradiated FeCrAl weldments and the controlling factors in their performance. In particular, resulting microstructure and postirradiation mechanical properties should be studied and determined. There is limited information on the performance of nonirradiated FeCrAl weldments [14,18], and very limited, if any, literature on the irradiated ones. Although FeCrAl alloys have primary been targeted for light water reactor fuel applications [19], the present work seeks to understand fundamental aspects on the radiation tolerance of FeCrAl alloys and their weldments. Thus, the current work broadens the scope to analyze the fundamental aspects of neutron irradiation at low damage dose (~2 dpa) on the properties and structure in the temperature range of 200°C to 550°C on various advanced FeCrAl alloys and alloys with laser-beam weldments.

2. Investigated Materials and Experimental Methods

2.1. Material fabrication and composition

The present work focuses on mechanical performance of the irradiated weldments of Generation II FeCrAl alloys [18], Table 1. Nonirradiated Generation I FeCrAl alloy weldments are discussed in [14]. Regarding Generation II, the alloying strategy, the material production routes, and element composition were presented in detail in [18], and only a brief overview of the fabrication and composition of the alloys is presented here. Alloy production included casting, homogenization at 1200°C in an argon gas atmosphere for 4 h followed by air cooling, and hot forging at 800°C with a 50% reduction in thickness (~25–~12.5 mm) to make plateshaped samples. The plates were then hot rolled at 800°C, with an additional ~40% reduction in thickness, and annealed at 800°C in laboratory air for 1 h. The final step consisted of warm rolling at 300°C with a 90% thickness reduction and annealing at 650°C for 1 h in the air [18].

Table 1. Composition (wt.%) of the investigated Generation II FeCrAl alloys

Alloy ID	**Short composition notation**	**Fe**	**Cr**	**Al**	**Y**	**Si**	**Nb**	**C**	**O**	**N**	**P**	**Ti**
C35M	Fe-13Cr-5Al	79.43	13.06	5.31	0.053	0.13	<0.01	0.001	0.0012	0.0003	0.007	<0.01
C37M	Fe-13Cr-7Al	77.49	13.01	7.22	0.081	0.19	<0.01	0.001	0.0026	0.0002	0.004	<0.01
C35M10TC	Fe-13Cr-5Al-1TiC	78.82	12.95	5.14	0.01	0.2	<0.01	0.18	0.0012	0.0007	<0.002	0.71

In all alloys, the amount of Mo is 2%. All other elements (Zr, B, Hf, V, W, Ce, Co, Cu, La, Mn, and Ni) were measured at or below <0.01; S < 0.0003.

An alloy designated as C35M (Fe-13Cr-5Al, in wt.%) was used as the reference material for this study. The C37M alloy was included to explore the effects of aluminum addition on welding-induced cracking and α' phase stability. Regina et al. [20] established a composition-based cracking boundary for FeCrAl alloys when using Gas Tungsten Arc Welding or Gas Metal Arc Welding techniques. Their data, presented in [20] and further discussed in [18], show that the base alloy, C35M, exists close to the proposed welding-induced cracking boundary. C35M also sits nearly on the phase boundary for the formation of the Cr-rich α' phase at moderate to low temperatures (≤475°C) [21]. The formation of the Cr-rich α' phase is detrimental because its presence has been linked to significant hardening and embrittlement of the alloy after aging or after high-flux neutron irradiation [22,23].

Note that the phase boundary offered in [21] and discussed in [18] was based on a change in the hardness of diffusion couple–like experiments after thermal aging at 475°C. Additionally, the compositions studied in [21] did not include Mo, which has been shown to increase hardening via α' precipitation [24]. Thus, it is possible that the phase boundary is not completely accurate at different conditions (e.g., temperature, radiation, minor alloy additions) and that the α–α' regime is larger (or smaller) than presented in [21], depending on exact conditions. Decreasing the end use/application temperature, such as the typical operating temperatures of light water reactors (~320°C), would also cause a shift in this boundary [25]. With this decreased temperature, it is predicted the C35M alloy would not be fully immune to precipitation of α' while in service. Hence, the inclusion of the C37M alloy in the test matrix enables the exploration of the delicate balance between the phase boundary and the weld-induced cracking boundary. The C37M alloy may exist outside the α–α' regime while still being resistant to welding-induced cracking.

The material with TiC addition (i.e., C35M10TC alloy) was introduced as a candidate alloy, as it is predicted the dispersion of TiC particles in the matrix may form efficient hydrogen trapping sites. These sites (i.e., small carbide or Laves phase particles) have been shown initially to reduce welding-induced cracking [20]. They could also act as pinning sites during recrystallization [26] or welding [15]; however, the effect of this addition on the in-reactor performance is unclear. Also, in the modified alloys, yttrium was added to enhance the oxidation resistance at elevated temperatures [27]. Molybdenum was kept at 2 wt.% to provide solution hardening of the body-centered cubic (bcc) matrix, which promotes strengths at elevated temperatures [19].

2.2. Laser-beam welding

Welding trials were completed using autogenous, bead-on-plate welding [18]. In all cases, the welding direction was transverse to the rolling direction (Figure 1). A pulsed laser welding machine was used to perform the welding. No preheating of the parts was conducted. Full penetration welds were accomplished using a 7 ms pulse length, with 7 pulses/s, and a 2.12 mm/s welding speed. Lamp energy was maintained near 100 W for the duration of the welding. All welds were performed with an argon shield gas covering both the top and bottom of the piece being welded. No post-weld heat treatment(s) were performed. More details on the welding procedure are given in [18].

The weldment surfaces and heat-affected areas were analyzed for porosity, visible nonmetallic inclusions, and cracks using an optic microscope with magnification up to 200×. No voids, rough inclusions, cracks, or other welding defects were observed at the surface. Several weldment cross sections per alloy were prepared for additional analysis using scanning electron microscopy-electron back scatter diffraction (SEM-EBSD); no cracks or pronounced porosity were observed on these cross sections. Using the described methods, all analyzed welds were determined to be free of superficial cracks or other weld-induced defects.

X-ray computed tomography (XCT) was used to characterize the microstructures in 3D, particularly to detect the presence of pores and internal cracks, if any were present. The measurements were performed using a Zeiss Xradia Versa 520 operated at 140 kV, 9W. A total of 3,201 projections were collected through a 360° rotation along the vertical axis with a 1 × 1 binning, yielding a 0.5686 µm pixel size on the collected images. Data visualization and segmentation were performed using Dragonfly PRO v3.0 software.

The grain structure of the material prior to and after welding, Figure 2, was analyzed using SEM-EBSD to provide more precise measurements of the grain size, texture (i.e., orientation), and grain shape compared with traditional optical microscopy [14]. All samples investigated were carefully polished using standard metallography procedures to produce a defect-free, mirror-like surface. Colloidal silica polishing was used as the last preparation step. EBSD analysis was conducted using a JEOL JSM 6500F SEM with a field emission gun equipped with an EDAX EBSD system. The accelerating voltage was 20 kV, and the working distance was 12–17 mm. The step size of the EBSD maps varied between 0.5 and 3.0 µm depending on the resolution needed for microstructural assessment. The camera was operated in a 2 × 2 binning mode at around 90–100 frames per second.

2.3. Irradiation

Tensile specimens—SS-J type with a gauge size of 5 × 1.2 × 0.5 mm and SS-Mini type with a gauge size of 3.55 × 0.8 × 0.4 [28]—were loaded into irradiation capsules designed to meet nominal target temperatures of 200°C, 330°C, and 550°C at a damaging dose of ~2 dpa. SS-J type specimens were designated for testing at a shielded hot cell facility, and SS-Mini type specimens were intended for advanced mechanical testing at the Low Activation Materials Development and Analysis (LAMDA) facility housed at Oak Ridge National Laboratory (ORNL) [29]. At least two specimens per alloy and condition (i.e., welded and nonwelded) and specimen type were contained within each irradiation capsule. Irradiations were conducted for the full duration of Cycle 465 in the High Flux Isotope Reactor (HFIR) at ORNL using the central flux trap facility. Since no active temperature control was employed, determination of final irradiation temperatures was completed by dilatometric analysis of passive SiC thermometry samples. The dilatometric analysis was conducted up to a maximum temperature of 600°C at a constant ramp rate of 1°C/min and a cooling rate of 2.5°C/min using a Netzsch 402 CD dilatometer and methodology described in [30].

Nominal irradiation temperature for each specimen was determined from SiC thermometry specimens contained within the same radial and axial stack of specimens within the capsule. Typically, SS-J type specimen stacks within the irradiation capsule ran at slightly lower temperatures (~30–40°C) compared with the SS-Mini tensile specimen stacks within the same capsule, a result predicted in [28]. This variance can be attributed to the higher average thermal contact resistance between the stack configuration of the SS-Mini type specimens over the SS-J type specimen stacks. The capsule mean irradiation temperature (CMIT) was determined from the mean of all thermometry tested within each capsule; radial and thermal gradients are not reflected in this value. The full details including final irradiation dose, neutron flux, and neutron fluence for each capsule are provided in Table 2. Variances in irradiation conditions are a by-product of the different positions of each capsule within HFIR's core.

Table 2. Summary of FeCrAl capsule irradiation conditions

Capsule ID	Temperature range ID*	CMIT (°C)	Dose (dpa)	Dose Rate (dpa/s)	Neutron Flux (n/cm2/s) E > 0.1 MeV	Neutron Fluence (n/cm^2) E > 0.1 MeV
FCAT-01	LT	194.5±37.9	1.9	9.8×10^{-7}	1.10×10^{15}	2.17×10^{21}
FCAT-02	MT	363.6±23.1	1.8	9.3×10^{-7}	1.04×10^{15}	2.05×10^{21}
FCAT-03	HT	559.4±28.1	1.9	9.8×10^{-7}	1.10×10^{15}	2.17×10^{21}

*LT: low temperature, MT: middle temperature, HT: high temperature

2.4. Mechanical test details

Tensile specimens, both SS-J and SS-Mini, were produced from the welded plates using an electric discharge machine (EDM). The fusion zone was in the center of the welded specimen gauge. After EDM cutting, the specimen blanks were mechanically ground to the final thickness.

Uniaxial tensile tests for the SS-J type specimens were completed within a shielded hot cell facility on an Instron universal test machine using remote operation. Shielded facilities were needed to complete testing due to the high level of radioactivity of the larger SS-J type specimens (≫100 mrem/h at 30 cm) at the time of this study. All tests used shoulder loading and a nominal strain rate of 10^{-3} s^{-1}. Cross-head displacement was digitally recorded to determine engineering strains. All tests were performed in ambient air. Due to the limited number of specimens available at the time of this study, only one specimen per configuration (i.e., welded and nonwelded) and irradiation condition was completed for the SS-J type specimens. A JEOL JSM-6010LA SEM, located in the shielded hot cell facility and remotely operated, was used to investigate the fracture surfaces of the SS-J type tensile specimens. Fractography was completed using a 5 kV beam at a 10 mm working distance.

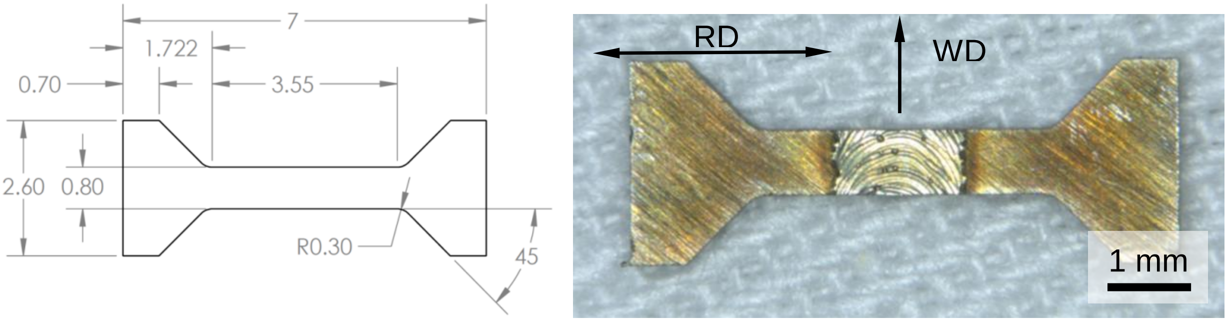

Figure 1. Tensile specimen geometry (SS-Mini type with 0.4 mm thickness) design for the present work (left) [28] **and appearance of the weldment on the specimen surface (right). The specimen is shown prior to the final mechanical grinding. SS-J type specimen geometry is also described in** [28]**; RD and WD labels show rolling (tensile) and welding (transverse) directions, respectively.**

Tensile tests with irradiated and nonirradiated SS-Mini type specimens (Figure 1) were performed at ORNL’s LAMDA facility on an MTS Insight 2-52 one-column tensile screw machine with a 2 kN load cell. This geometry was developed for the present work [28] to conduct out-of-hot cell testing of the irradiated welded specimens. It was important to evaluate the properties of the irradiated weldments in detail using advanced experimental approaches like digital image correlation (DIC) (see below), and, as believed, the SS-Mini type specimen geometry suited this goal well enough. The tensile specimens (one irradiated and three to five nonirradiated specimen per alloy and condition) were shoulder loaded and tested at room temperature with a nominal strain rate of 10^{-3} s^{-1}.

SS-Mini type specimens were designed to mimic the behavior of the SS-J type specimen geometry [28]; engineering mechanical properties defined by using these geometries are close enough for bulk, nonwelded material [28]. However, for the welded specimens some deviation may be expected depending on the geometry. This aspect is discussed in detail in [31] for nonirradiated weldments.

Before the tensile tests, the SS-Mini type specimens were painted with a random speckle pattern. The surface speckle pattern allows for optical, noncontact strain measurements using a DIC approach [32]. This method is now a common research tool employed by many research teams [33–38] for strain measurements, visualization of deformation bands, and necking analysis; however, at the moment there is limited literature for irradiated materials. Regarding weldment performance analysis, DIC provides for the possibility of measuring the local yield stress (LYS), retrieving local strain values [17,37,39], and calculating local true strain–true stress curves. The features and limitations of DIC are widely described in the literature [32] and will not be discussed here.

A high-resolution Allied Vision GX3300 camera equipped with a telecentric lens was used in the experiments reported here; the lens provided a resolution of around 5 μm per pixel. Strain fields and true stress–true strain curves were calculated using VIC-2D commercial software and a custom application. The DIC data were used to calculate LYS values along the specimen gauges; the LYS values show strength level at a particular location and are especially useful for welded specimens [37,39] with property gradients. The analysis of LYS is a relatively new concept; its advantages and possible issues are analyzed by a number of authors [37,39]. Strain rate maps were employed to investigate the distribution and evolution of localized deformation. This approach [40] allows for the compact and efficient representation of a large amount of data; yield stress initiation, necking, and strain localization may be easily seen in a color-graded image [40]. DIC results were employed to estimate the plastic anisotropy degree [41,42] of the as-received (AR) and welded specimens before and after irradiation.

3. Experimental Results and Discussion

3.1. Structure of the nonwelded and welded alloys prior to irradiation

Figure 2 shows the typical microstructure and texture of the AR alloys and the microstructure of the weldments. The AR alloys showed a microstructure consistent with warm-rolled material conditions, with a mix of deformed (i.e., nonrecrystallized) and recrystallized grains. All alloys exhibited strong texturing near the [101] corner of the unit triangle with respect to the warm-rolling direction, which was also the tensile direction. The recrystallized grains, as a rule, had a close-to-random texture, with the C37M alloy being the best example (Figure 2, middle row). However, sometimes the chains of recrystallized grains had a similar orientation (see color in inverse pole figure [IPF] map). Such chains could potentially lead to decreased mechanical performance. A similar case, with detrimental texturing and ridging due to the presence of coarse-grain chains (i.e., “streams”), was discussed in [43] for a ferritic steel with 11 wt.% of Cr.

The recrystallization degree varied for the investigated AR materials of a nominally identical processing route. The C35M alloy experienced moderate recrystallization, whereas C37M demonstrated an almost fully (>90%) recrystallized structure with well-shaped grains (Figure 2). Recrystallization was less pronounced in the C35M10TC alloy with the TiC additions, compared with the other investigated alloys. The size of the recrystallized grains was significantly smaller in this alloy, when compared with C35M and C37M, suggesting the TiC has a positive effect on grain refinement. Small variations in the composition may lead to significant changes in the recrystallization kinetics [44] and final grain size of these alloys (e.g., C35M vs C37M, as shown in Figure 2).

EBSD maps across the length of the weldment were generated and then stitched together to provide a full field of view of the weldment grain structure. Figure 2 shows the structure of the investigated alloys’ weldments. For the C35M and C37M alloys, welding led to the formation of relatively large grains of irregular shapes near the weldment centerline. This feature was complemented by elongated or columnar grains that appeared roughly 200–300 µm away from the centerline. The width of the columnar grain area was around 300 µm. Distinct areas of coarse, round-shaped grains were observed nearly 600 µm away from the centerline.

The welded C35M10TC alloy had a distinctly different microstructure in the fusion zone compared with other materials. The grain size of the fusion zone was significantly reduced and was on the order of 3–5× smaller. The grains near the weldment centerline had specific morphology with torturous boundaries (Figure 2). The columnar grain area was also smaller, and grains appeared to be more elongated. Additional details may be found in [18].

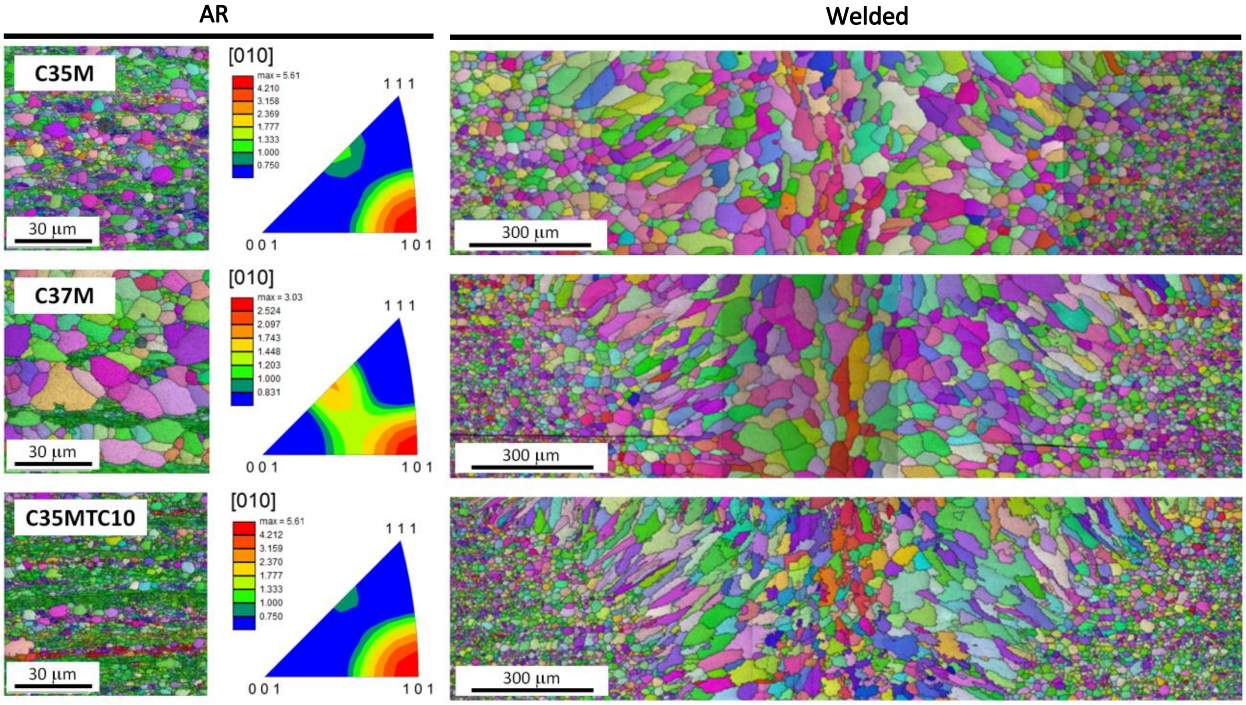

Figure 2. The structure and texture of the as-received (AR) alloys (left) and microstructure of the weldments (right). The IPFs are colored, and the texture plot for the AR specimens is oriented in the tensile direction. Note the larger magnification level in the IPF maps at the left.

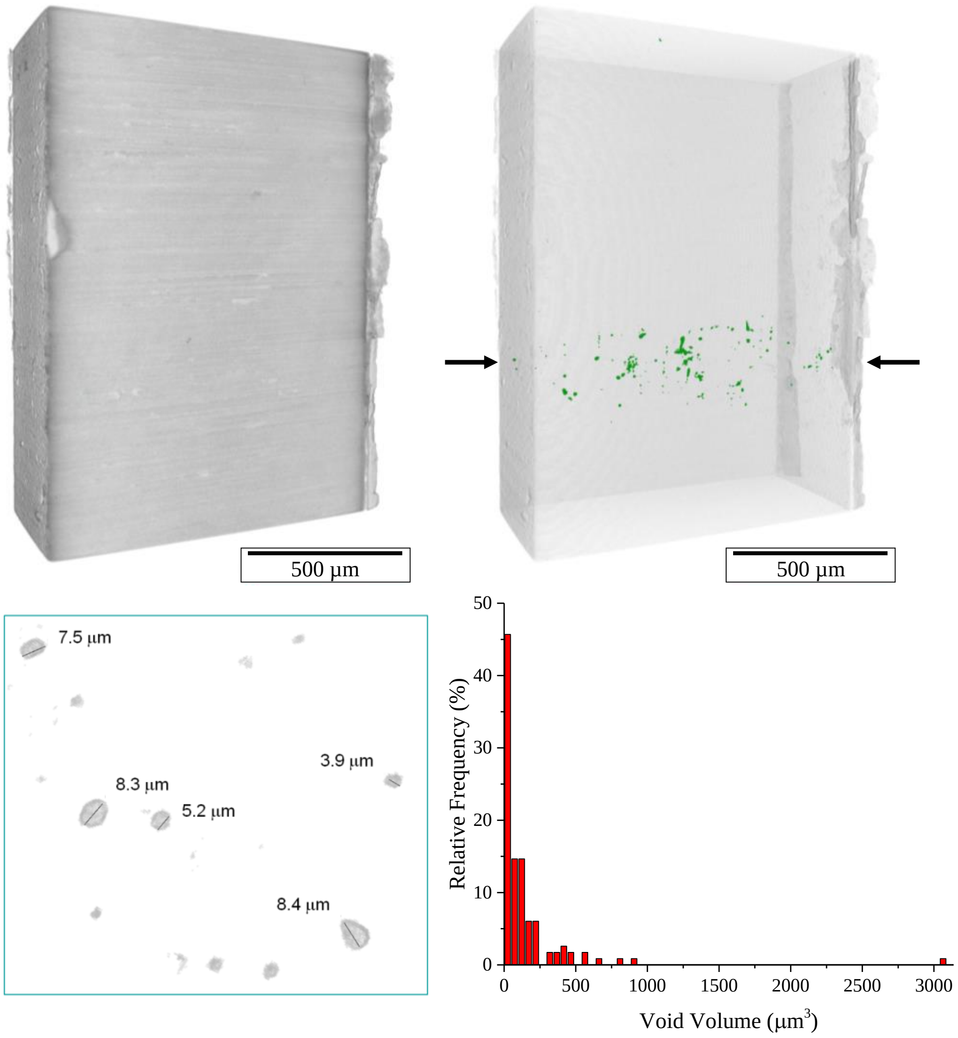

Figure 3. (Top row) Scanned gauge of the nontested C35M alloy tensile specimen (left) and voids appeared in the XCT data set; the arrows show the approximate location of the weldment centerline. (Bottom row) 2D slice showing the specific distribution and dimensions of some of the largest voids (left) and the void volumes presented as a function of their relative frequency, obtained from the segmented data.

The XCT results from the C35M alloy are presented in Figure 3. The 3D reconstruction of the scanned part is shown on the top row, with the segmented voids highlighted in the image at top right. The two arrows show the approximate location of the weld line. The voids are thought to be the gas porosity introduced during welding. A sliced 2D image showing some of the largest voids observed is presented at bottom left, with the longest dimensions marked. The calculated void volumes as a function of their relative frequency (obtained from the segmented data) are presented at bottom right, indicating most of the pores were below 100 µm^3 (or less than ~10 µm in size).

3.2. Engineering tensile curves and mechanical properties before and after irradiation

Representative engineering tensile curves for the investigated alloys in the irradiated and nonirradiated conditions are shown in Figure 4. Nonirradiated, nonwelded specimens of all alloys showed nearly identical tensile behavior: a smooth transition from elastic to plastic deformation, sometimes with very weak force drop near the yield point, moderate deformation hardening, and pronounced necking. Strength and ductility level were comparable for all nonirradiated alloys, and the SS-Mini type test results agreed well with the more common SS-J type specimen geometry, as discussed in detail in [28].

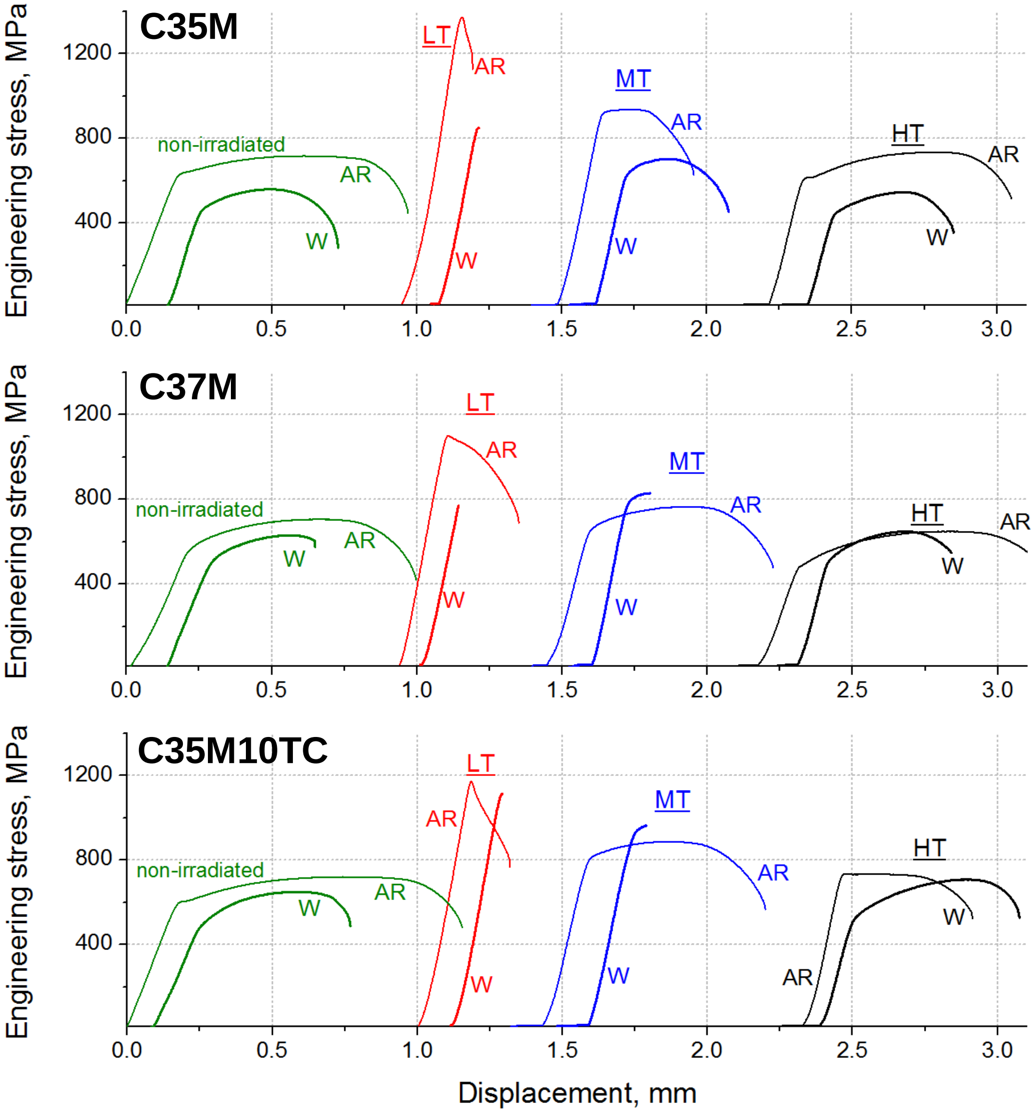

Figure 4. Raw engineering tensile curves for irradiated and nonirradiated specimens of the investigated FeCrAl alloys (SS-Mini type geometry). LT, MT, HT: low, middle, and high temperature; AR: as-received material; W: welded specimens. See Table 2.

Nonirradiated weldments had slightly lower yield stress and significantly lower ductility; however, the difference in ductility came not from the weldment properties but from the fact that the welded specimen is a complex object with multiple different property areas [39]. Welding-induced softening was caused by altering the warm-rolled structure and grain growth during solidification within the fusion zone of the weldment [18]. While yield strength of the nonirradiated welded specimens varied slightly among the materials investigated here, the ductility response demonstrated more pronounced changes. In particular, the C37M alloy specimens showed lower ductility, compared with other alloys, and very weak necking. Earlier, the C37M alloy revealed strongly decreased ductility of the weldment [18], most likely due to preexisting defects.

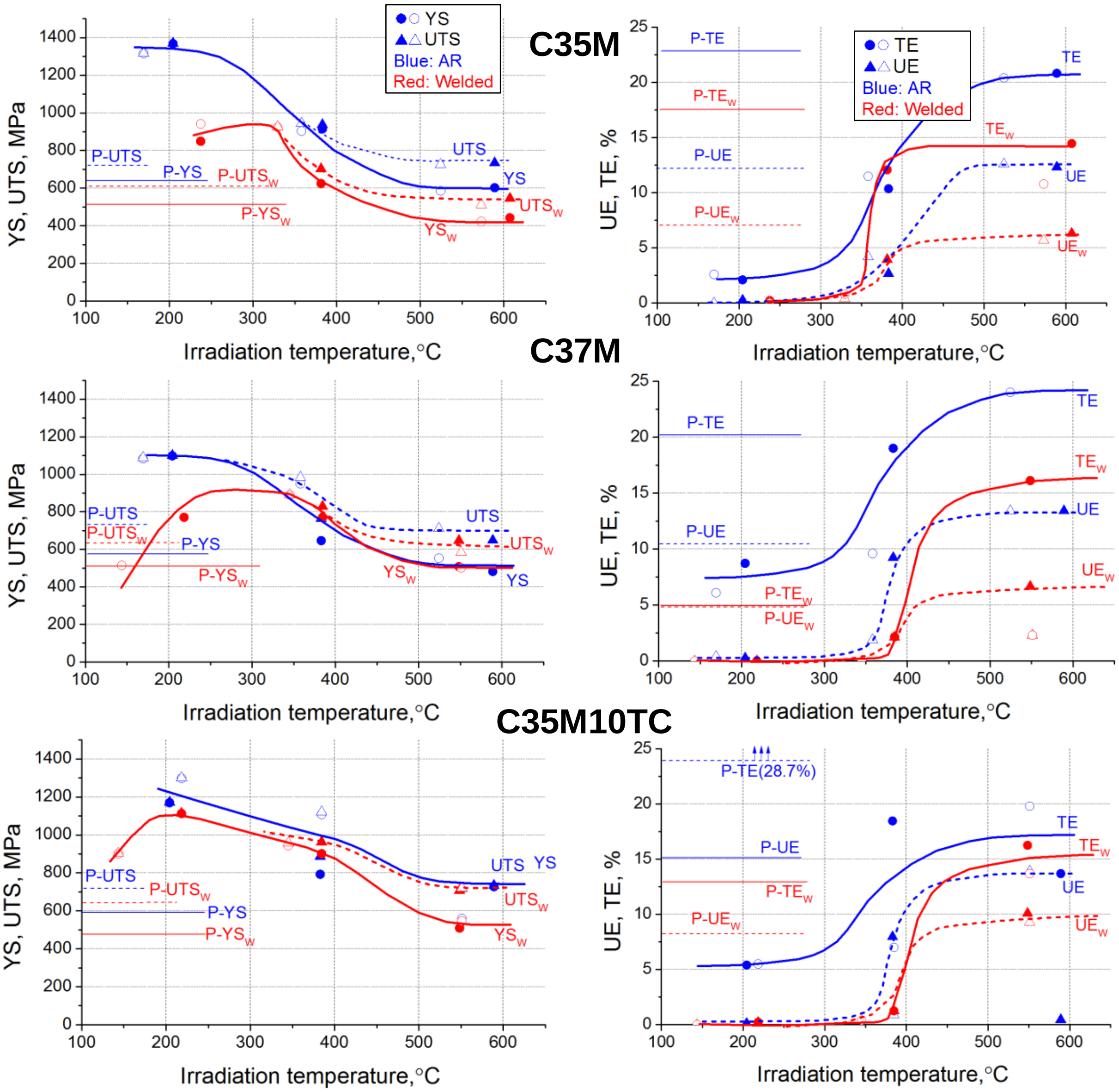

Figure 5. Mechanical properties—yield (YS) and ultimate tensile (UTS) stress, uniform (UE) and total (TE) elongation—for the investigated alloys as a function of the individual specimen irradiation temperatures. Open and closed symbols show data points for SS-J and SS-Mini type specimen geometries, respectively. Blue: as-received (AR) or parent material; red: welded specimens. Thin horizontal lines at the left and labels with P-prefix represent the baseline data for the AR and welded specimens prior to irradiation. The tests were performed at room temperature. Spline fits added to aid the eye of the reader.

Neutron irradiation led to pronounced changes in the strength and ductility of tested materials (Figure 4). Low-temperature (LT) irradiation—CMIT of 194.5±37.9°C—eliminated uniform elongation for nonwelded specimens; however, pronounced necking still developed. The impact of the LT irradiation on the welded specimens was more severe. Both uniform and localized deformation practically disappeared, and the tensile curve showed mostly elastic deformation.

The moderate-temperature (MT) irradiation had a modest ductility decrease (i.e., embrittlement) and a hardening effect on the parent (i.e., nonwelded) specimens but led to embrittlement of the welded ones. The welded C35M alloy specimens still demonstrated some plasticity, but other alloys revealed severe degradation of full and total elongation.

In contrast to the LT and MT conditions, the high-temperature (HT) irradiation revealed very weak radiation hardening effects, with only C35M10TC demonstrating some increase in the stress levels, and did not show degradation in the ductility when compared with the nonirradiated specimens.

Figure 5 shows mechanical properties of the investigated alloys in the AR conditions and after welding as a function of the irradiation temperature. The results are plotted as a function of the irradiation temperature determined for each tensile specimen based on the closest irradiation temperature value defined from an individual SiC thermometry specimen. Thus, the actual irradiation temperature for different tensile specimens varied slightly from CMIT values (Table 2) due to the axial and radial thermal gradients under irradiation. Using the individual specimen irradiation temperature spreads the data points along the x-axis, and instead of three nominal irradiation temperatures, one had up to six temperatures per irradiation capsule (i.e., three SS-Js and three SS-Minis), allowing for more detailed and accurate analysis of the role of irradiation temperature on mechanical performance.

Results show that pronounced radiation hardening and embrittlement exist for LT irradiation (below 250°C) for all alloys; uniform elongation values dropped practically to zero for all specimens. Welded specimens also had close to zero total elongation. It is important to emphasize, when the irradiation temperature was similar for the SS-J and SS-Mini type specimens, these geometries, as a rule, delivered comparable results for nonwelded specimens; the largest deviation was observed for the MT range, most likely due to the irradiation temperature fluctuations.

Interestingly, welded specimens of C35M and C37M alloys showed smaller radiation hardening (i.e., an increase in the yield stress) during LT irradiation, compared with AR material. This effect is most likely due to varying kinetics in α' precipitation and dislocation loop formation between the large random-oriented grains within the fusion zone versus the more fine and textured grains within the parent material. For example, both the grain boundaries and the dislocation networking have been shown to influence the ratio of dislocation loop types (e.g., Burgers vectors of $a/2\,\langle 111\rangle$ or $a\langle 100\rangle$), the local size of the dislocation loops, and the number density [45]. Additionally, Capdevila et al. [46] investigated the precipitation kinetics of α' in an as-hot-rolled and recrystallized FeCrAl and showed faster α' phase accumulation kinetics within the as-hot-rolled microstructure. Changes in the number density and size of both dislocation loops and α' have been determined to have significant influence on the hardening behavior of FeCrAl alloys [47]. Here, it is speculated that a similar effect is occurring where faster kinetics in α' precipitation in the base metal promotes greater hardening within the parent material when compared with the fusion zone of the weldments, but further characterization is needed to conclusively determine if this is indeed the case.

The MT irradiation (300–400°C) showed some radiation hardening and a modest decrease in ductility in the three FeCrAl alloys. Hardening in the C35M specimens was more pronounced compared with the C37M specimens, likely due to the differences in the α' phase formation under irradiation. At the same time, the C37M and C35M10TC alloy weldments demonstrated more severe embrittlement, compared with the C35M alloy. The HT irradiation (>500°C) did not show any visible radiation hardening for C35M and C37M alloys, with a weak increase in stress level for C35MTC10 alloy. Analyzing the ductility changes in Figure 5, one may see the tendency of radiation embrittlement disappearance if irradiation temperature exceeds ~380–400°C. These results agree well with the literature data for some bcc materials; for example, for ferritic steels, like F82H, radiation effects reducing ductility become negligible if irradiation and test temperature exceeds ~380°C [48].

3.3. Analysis of the deformation behavior using DIC data

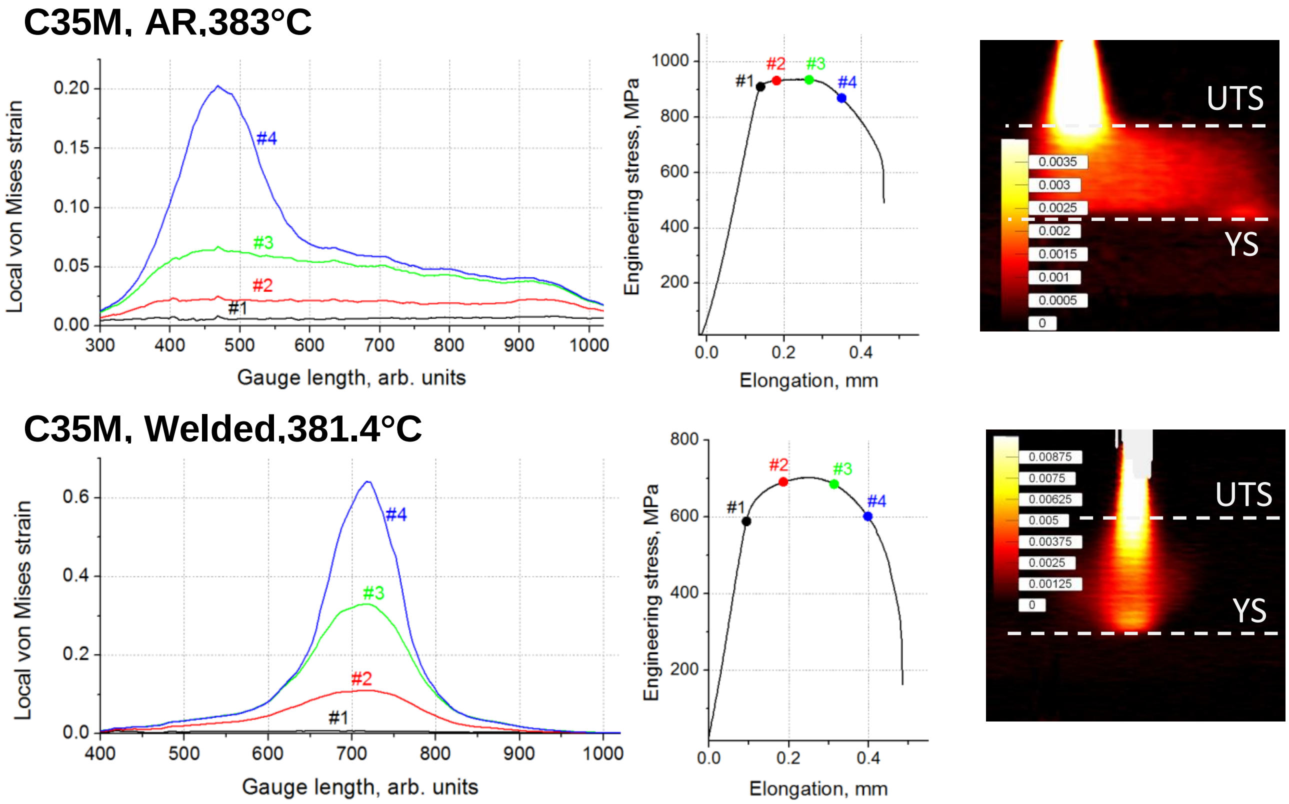

Figure 6. (Left) local strain distribution (von Mises strain, Green-Lagrange strain tensor definition) along the irradiated specimen gauge at different global strain levels. (Middle) Engineering tensile curves; C35M alloy specimens irradiated at MT range. (Right) Strain rate maps depicting local strain rates along the gauge during the experiment.

Figure 6 shows the DIC results for several irradiated specimens: local strain distribution along the gauge at different “global” strain levels [39] and local strain rate maps. One may see that near the yield stress point (curve #1), mostly elastic uniform strains are present in the specimen. As strain and stress is increased, uniform deformation is developed (curve #2) in the nonwelded specimen. Near the ultimate tensile stress (UTS) point, a small inhomogeneity in the strain distribution appeared (curve #3), with slightly larger strains at the left side. After that, necking developed (curve #4 in Figure 6, top left). The strain rate map shows uniform deformation as an “orange” area (strain rate ~0.001 s^{-1}); no visible strain occurred below the yield stress limit. Close to the UTS, deformation localized in the neck, with local strain rates being ~3–5 times larger compared with the nominal value.

This kind of behavior—initial close-to-uniform straining with final necking—was observed for all nonwelded specimens. After irradiation, uniform strain might have disappeared; if this had occurred, the strain rate map would have demonstrated only necking (i.e., fast local straining). However, in the present study, the welded specimen demonstrated a completely different behavior. After yield stress (point #1), one may expect some uniform deformation, judging from the tensile curve shape. However, welded specimens consistently revealed a bell-like (or delta-like) strain distribution with strain maximum at the weldment centerline. As deformation progressed, curves #3 and #4 in Figure 6 (bottom left) show that necking always developed at the weldment center. Strain rate maps for the welded specimens show increased strain rates in the weldment center. In other words, most of the plastic strain was isolated within the fusion zone of the weldment, whereas neck and fracture locations were random in the parent AR material.

3.4. Plastic anisotropy before and after irradiation

Plastic anisotropy is rarely discussed with respect to a material's deformation behavior. However, this parameter may be important for the final products, for example, for nuclear fuel cladding tubes and ducts, reflecting the ratio between thinning (i.e., the change in wall thickness) and shortening (i.e., the decrease in tube length) during ballooning or burst behavior [41,42].

Plastic anisotropy is usually defined as follows. If the specimen is being loaded above yield stress in the x-direction, it will experience elongation (i.e., plastic strain) in the x-direction (defined as ε_x) and contraction in the y- and z-directions (i.e., ε_y and ε_z, respectively); see Figure 7 inset. For the perfectly isotropic material, $\varepsilon_y = \varepsilon_z$, but this is not always the case. Crystallographic texture and/or a limited number of slip systems may lead to the anisotropic behavior ($\varepsilon_y \neq \varepsilon_z$) of the sheet or tubular product [41,42,49]. One may speculate that neutron irradiation can also change the plastic anisotropy of the material by limiting the number of active slip systems and stimulating deformation localization via dislocation channel formations.

Several approaches describe plastic anisotropy, including the Lankford coefficient ($R_x=\varepsilon_y/\varepsilon_z$) and the R- and P-parameters [42]. In the context of the present work, since DIC data were available, it seems reasonable to discuss the ε_y and ε_z values as a function of tensile strain, ε_x. Engineering strains (or Cauchy strains, $\Delta L/L_0$) in the tensile (ε_x) and transverse (ε_y) directions are natural outcomes of the tensile test if DIC is employed. To ensure reliable results, it is important to make sure the shear strains are small, the specimen experiences no rotation, and deformation bands are absent or weak. Then, if the volume remains constant during plastic deformation [i.e., $(1+\varepsilon_x) \times (1+\varepsilon_y) \times (1+\varepsilon_z) = 1$], one may express the strain across the thickness as $\varepsilon_z = 1/((1+\varepsilon_x)(1+\varepsilon_y)) - 1$. If the Hencky strain (or natural strain) definition is employed, an even simpler relationship may be used, $\delta_z = -(\delta_x+\delta_y)$.

Figure 7 shows values for the ε_y (i.e., transverse strain) and ε_z (i.e., strain across the thickness) as a function of the strain in the tensile direction, ε_x, for C35M specimens prior to and after irradiation. The elastic strain was not excluded, but it was small enough (<~0.005). One may see that the nonirradiated specimens had strong anisotropy; strain value across the thickness (ε_z) was significantly large compared with the ε_y, which may be explained by the texture in the material (see Section 3.1). Irradiation did not change the general behavior but slightly changed the ratio between ε_z and ε_y.

Welding led to the decrease of plastic anisotropy, most likely, because the preexisting texture disappeared after welding. The irradiated weldment did not reveal strong plastic anisotropy when compared with the nonirradiated weldments. One may conclude that, for the investigated dose range (1.9 dpa), the preexisting texture is the main factor controlling plastic anisotropy.

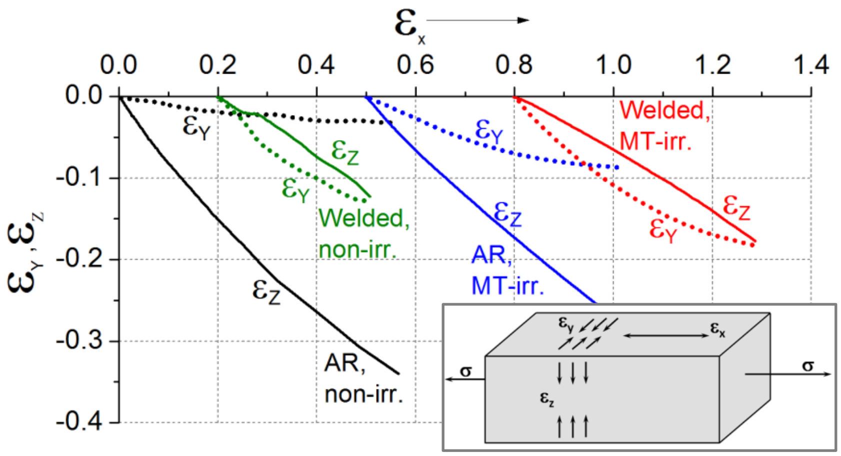

Figure 7. Plastic anisotropy—the ε_y and ε_z strains as a function of the ε_x strain—for the as-received (AR) and welded specimens of C35M alloy before and after MT irradiation. Negative strain values reflect a contraction in the y- and z-directions. Curves for different specimens are shifted along the x-axis to improve image readability. The inset at bottom right defines the axes, where the x-axis corresponds to the tensile direction.

3.5. Fracture mechanisms in the irradiated specimens

Figure 8 shows the typical fracture surfaces for the irradiated AR and welded SS-J type tensile specimens; because the behavior of the alloys tested was very similar, only the C37M alloy data set is shown. The nonirradiated AR specimens of all alloys demonstrated a ductile fracture mechanism during tensile testing [18]; after irradiation at 1.9 dpa, the AR specimens also revealed a ductile fracture mechanism (Figure 8). Ductility is likely to change with increasing damage doses, as mechanical property data on similar model FeCrAl alloys showed that irradiations performed between 320 and 382°C at doses below 7 dpa are still within the transition regime for mechanical performance [47]. Irradiation temperature played a secondary role at the investigated damage dose; however, LT-irradiated AR specimens often revealed small secondary cracks (Figure 8, white arrows at top left).

After welding, the C35M alloy demonstrated mostly ductile fracturing prior to irradiation, as discussed in [18]; no cleavage spots were observed. In contrast, after irradiation, the alloy had completely brittle fractures; only cleavage surfaces were observed. Welded C37M alloy revealed brittle fracture before [18] and after irradiation (Figure 8); no ductile dimples were detected.

Interestingly, the cleavage fracture mechanism (Figure 8) did not interfere with the high local ductility and neck development for the welded specimens prior to irradiation and after HT irradiation (Figure 5 and Figure 6). One may speculate that fractures occurred only after reaching some stress level threshold. In other words, below some critical stress level, the material should reveal acceptable performance. Additionally, an interesting aspect is the complex character of the fracture and the appearance of multiple secondary cracks in the welded specimens. In some cases, small particles and debris are clearly visible in the SEM images (Figure 8, black arrows at top right).

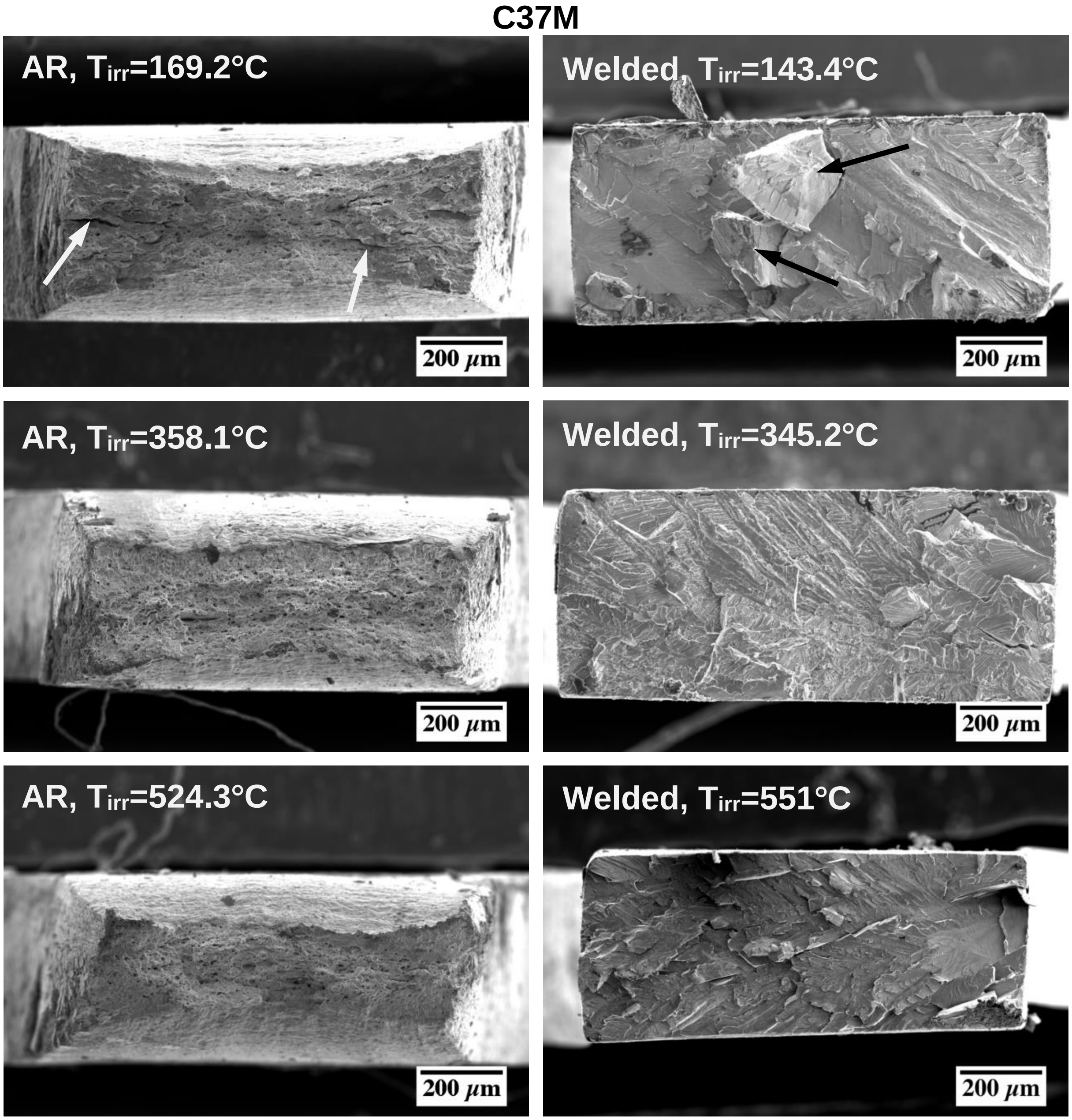

Figure 8. SEM images of the fracture surface of SS-J3 type specimens. Irradiation temperature is given for every object. One may see brittle fracture for the welded specimens. White arrows show secondary cracks for LT-irradiated specimens. Black arrows point to debris particles. AR: as-received material. $_{irr}$ **indicates irradiation temperature.**

3.6. True stress–true strain curves for the nonirradiated and irradiated specimens

To investigate the behavior of the weldment and the bulk material in more detail, the local mechanical behavior was analyzed in terms of true stress–true strain curves using DIC data for the welded and AR specimens. True stress–true strain curves were calculated using common approaches [37] to assess the material behavior prior to and after welding, as well as prior to and after irradiation. This type of curve has no UTS point or uniform elongation limit, and the true curves end at specimen fracture. During the experiment reported here, the maximum strain value was limited to some degree due to limitations inherent in the experimental method used to retrieve the true curves. For example, with the DIC approach as the main tool, inaccuracy increases when necking begins or when a complex stress state forms [39]. It is possible to overcome this limitation and get a true stress–true strain curve for the neck by combining DIC and finite element modeling [36]; however, this option is difficult to use with the welded specimens [39]. Additionally, detailed analysis of the true curves usually includes some constitutive equations [50] or modern approaches based on the physics of plasticity [51], but this aspect was outside the present work scope.

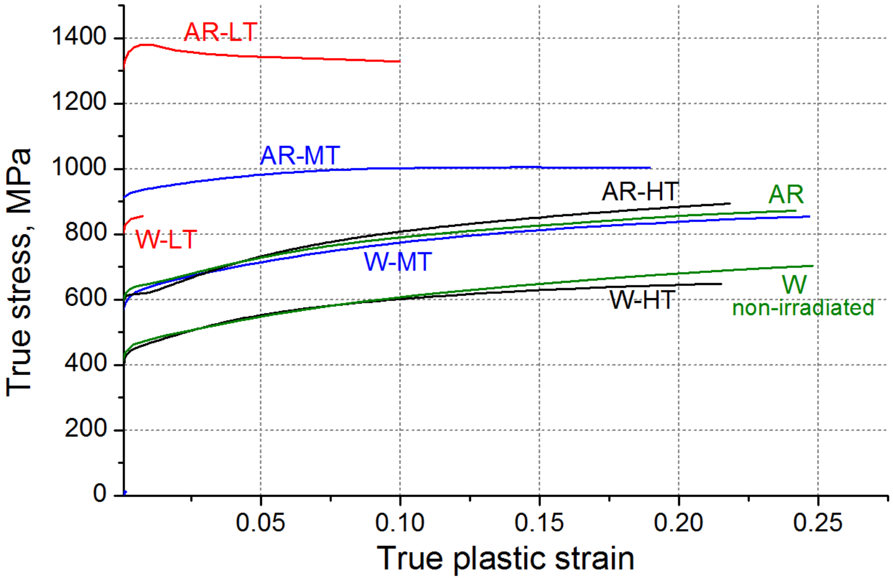

Figure 9. True stress–true strain curves for C35M alloy. Only plastic strain is shown; elastic deformation was excluded. AR and W: as-received and welded specimens, respectively. LT, MT, HT: low, moderate, and high temperature.

Figure 9 shows the calculated true strain–true stress curves for the C35M alloy before and after irradiation. The curves were calculated for the bulk AR material and the fusion zones (i.e., ~300 μm central areas of the weldments). A wide range of curves may be obtained for the grain growth area and heat affected zone (HAZ), reflecting a smooth transition of properties from weldment center to the parent material. However, for the sake of simplicity, only ultimate cases (AR bulk material vs weldment center) will be analyzed.

For the nonirradiated specimens, welding of the AR material shifts the true stress–true strain curves to lower stress levels. The kinetics of strain-induced hardening remains almost unaffected by the welding, and the difference between the AR and welded specimens is practically the same (~200 MPa) through the studied strain range. HT irradiation did not lead to any significant changes in the appearance and shape of the true stress–true strain curves.

MT irradiation led to the radiation hardening for both the AR and welded specimens. The curve for welded specimens appears to have shifted in the high-stress area at ~180 MPa; however, its shape remains similar to the curve for nonirradiated specimens. At the same time, the AR specimen demonstrated different behavior. As stress increased, the deformation hardening rate decreased and became close to zero at ~0.10 of plastic strain. Saturation of the deformation hardening was not observed in the nonirradiated or HT-irradiated specimen in the studied strain range, 0–0.2.

LT irradiation led to pronounced radiation hardening, with yield stress reaching ~1300 MPa for the AR material. The welded specimen demonstrated strong embrittlement, and the maximum plastic strain value did not exceed ~1% (0.01). The most interesting case was the AR specimen: It revealed strain-induced softening (i.e., decrease in the true stress) starting at strain levels of ~0.015.

Generally, the true stress–true strain curves contain several stages. In the small strain area (roughly, 0 to ~0.01), one may observe strain-induced hardening for all specimens. After that, the strain-induced processes were sensitive to the irradiation temperature, softening for LT irradiation and hardening for MT and HT irradiation). Additionally, one may speculate that being continued to the large strain area, the curves eventually saturate at some stress level (e.g., ~1000–1100 MPa). Further analysis of strain-induced processes should include evaluation of the structure; the focus should be on the α' phase formation and its interaction with dislocations. This aspect will be addressed in the future.

3.7. Local yield stress evolution under irradiation

As mentioned above, a miniature welded specimen is a complex object with multiple domains (e.g., weldment, HAZ, parent material; see Figure 1). These domains are expected to have different properties [39,41]. In most cases, if no aging occurs, yield stress calculated from the engineering tensile diagrams (Figure 4) represents the strength of the weakest location, which is usually but not neccessarly the center of the fusion zone, and misrepresents the overall plastic behavior of the tested specimen. If data analysis is limited by engineering curves only, the properties of other areas like the HAZ remain unexplored. In some cases, local mechanical properties of the weldment and the HAZ may be studied if one tests miniature specimens extracted, for example, directly from the weldment [52]; however, it is difficult to do for the narrow (~1.5 mm) weldments used here (Figure 1).

In the present work, LYS distribution curves were calculated for the tested irradiated and nonirradiated specimens using DIC data. The procedure used here was close to the approach offered and evaluated in [17,39]. To retrieve the LYS curves, the approach evaluates the transition from purely an elastic behavior to an elastic–plastic behavior for each point [17,39] along the specimen gauge, using DIC images collected during the test [37].

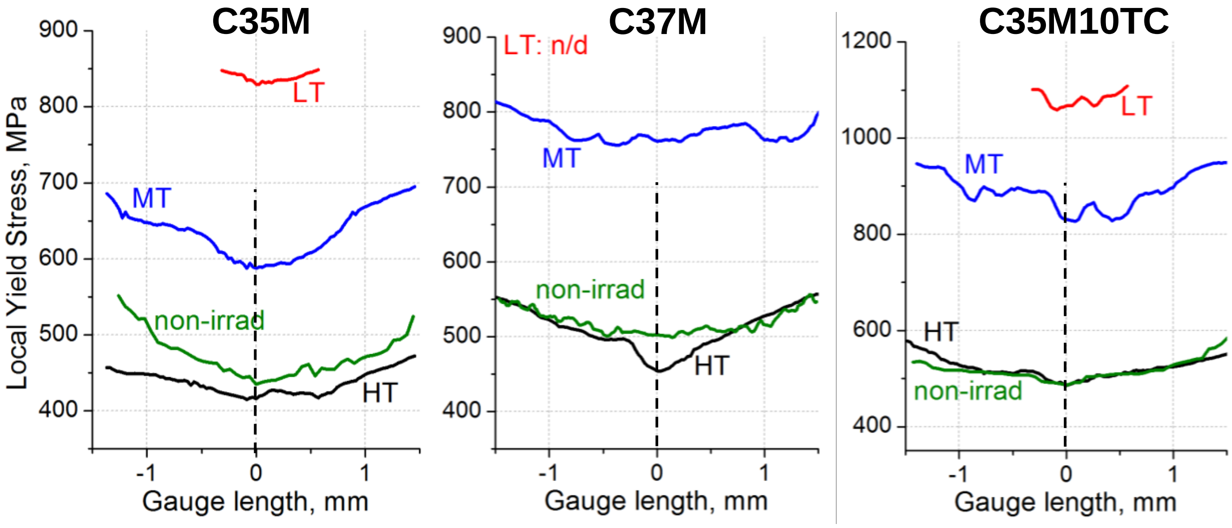

Figure 10. LYS distributions along the specimen gauge centerline. The zero position on the x-axes (black dashed line) corresponds to the center of the weldment, which is also gauge center. Gauge length is 3.55 mm for this specimen geometry; the portions of the LYS curves adjacent to the gauge ends were cut to avoid head influence. The welded specimen of C37M alloy demonstrated brittle fracture without any signs of plastic deformation.

Figure 10 shows the distribution of the LYS along the specimen gauges. As shown in the data, in all cases, the minimum LYS values correspond to the weldment center with the largest grains. The presence of small voids (Figure 3) in the weldment center may be an additional factor decreasing LYS at this location. The LYS curves had a specific “U”-like shape, and LYS values in most cases increased with distance from the weld centerline. Weak fluctuations on the curves were caused, most likely, by local variations in the grain size.

The LT-irradiated specimens demonstrated plastic deformation in a narrow, very limited area; specimen fracture prevented the plastic strain from spreading along the gauge. In this case, DIC data contained mostly elastic strain information, and it was not possible to calculate LYS curves for the whole gauge.

If a specimen with a long enough gauge had been tested, the LYS curves would demonstrate the smooth transition from the soft material in the weldment center through HAZ with the moderate strength to the parent material, unaffected by welding [17]. However, in the specimen geometry employed here, the small 3.55 mm gauge contained only a weldment and some portion of the HAZ. Thus, LYS curves did not reach the values obtained for nonwelded specimens (Figure 5).

Irradiation did not change the shape and appearance of the LYS curve but shifted them along the y-axis, reflecting the local radiation-induced hardening. Interestingly, the radiation hardening (i.e., the difference between the LYS curves for the reference nonirradiated specimen and the irradiated one) appears to be insensitive to the initial local strength of the material.

4. Summary and conclusions

FeCrAl alloys are promising materials for nuclear applications due to their better performance during LOCAs, compared to Zr-alloys. In the present work, advanced Generation II FeCrAl alloys were investigated before and after neutron irradiation. Laser-beam welded and reference tensile specimens were irradiated at ~1.9 dpa in ORNL's HFIR for a wide temperature range, from ~200 to ~560°C. All nonirradiated alloys revealed good weldability and were free of welding-induced cracking. Small voids were detected via x-ray tomography, but void density and size were small enough to be of limited concern. Weldment ductility and fracture behavior before irradiation strongly depended on the alloy composition. Whereas the C35M alloy weldment had a good ductility level, the Al content increase, from ~5% in C35M to ~7% in C37M, was detrimental even prior to irradiation leading to the ductility drop.

LT neutron irradiation (~200°C) led to the strong embrittlement of the weldments for all alloys; however, the AR materials still had ductility and pronounced necking. MT irradiation (~360°C) revealed strong embrittlement for the C37M and C35M10TC alloy weldments; it appears that Al and TiC additions were detrimental to the overall mechanical performance of the irradiated weldments. However, C35M alloy weldments still had ductility after MT irradiation. HT irradiation (~560°C) had little effect on the properties, which remained virtually unchanged except for C35M10TC alloy; it showed some weak radiation hardening. The summary results on the mechanical behavior suggest that a ductile-to-brittle transition occurs at ~380–400°C for all alloys, most likely due to the α' phase formation during irradiation below this temperature.

The present work results are also an important milestone in evaluating and comparing the specimen geometry performance. Ultraminiature specimen geometry (i.e., SS-Mini) was offered to perform out-of-hot-cell-instrumented mechanical testing soon after neutron irradiation to eliminate or reduce the postirradiation cool-down time; in the future, SS-Mini type specimens will be employed for in situ testing. There was, in general, good agreement in the mechanical test results between the common SS-J type and newly proposed geometry for the nonwelded irradiated specimens. A visible difference was observed for the ductility values for the welded specimens due to their complex structure and presence of multiple different property areas within the gauge. Thus, the pilot results for the irradiated weldments of advanced FeCrAl alloys showed the fruitfulness of the instrumented mechanical testing approach, justifying further efforts in this direction.

Additionally, out-of-hot cell testing allowed for the performance of deformation experiments using the DIC approach. Noncontact strain measurements via DIC allowed for development of a unique data set for irradiated FeCrAl alloys: true stress–true strain curves, LYS distribution within the irradiated weldments, and plastic anisotropy. DIC tests conducted with new geometry specimens revealed that plastic strain tends to localize in the weldment center, which was the weakest location for all alloys under the irradiation conditions in this study. The plastic anisotropy was weakly sensitive to the irradiation but was heavily affected by welding.

Acknowledgments

This research was sponsored by the US Department of Energy, Office of Nuclear Energy (DOE-NE), for the Nuclear Energy Enabling Technologies program for the Reactor Materials effort. A portion of the irradiation campaign, including capsule opening and radioactive specimen handling, was sponsored by the DOE-NE, Advanced Fuel Campaign of the Nuclear Technology Research and Development program. Authors would like to thank Dr. D. Hoelzer (ORNL) for fruitful discussion of the results and reviewing the paper, L. Varma (ORNL) for valuable help in manuscript preparation, and the Irradiated Materials Examination and Testing facility and LAMDA laboratory staff for their continuing support of this research.

This manuscript has been authored by UT-Battelle, LLC, under Contract No. DE-AC05-00OR22725 with the U.S. Department of Energy. The United States Government retains and the publisher, by accepting the article for publication, acknowledges that the United States Government retains a non-exclusive, paid-up, irrevocable, worldwide license to publish or reproduce the published form of this manuscript, or allow others to do so, for United States Government purposes. The Department of Energy will provide public access to these results of federally sponsored research in accordance with the DOE Public Access Plan (http://energy.gov/downloads/doe-public-access-plan).

References

[1] K. Murty and I. Charit, "Structural materials for Gen-IV nuclear reactors: Challenges and opportunities," *Journal of Nuclear Materials*, vol. 383, 2008, pp. 189–195.

[2] P. Yvon and F. Carré, "Structural materials challenges for advanced reactor systems," *Journal of Nuclear Materials*, vol. 385, 2009, pp. 217–222.

[3] K.A. Gamble, T. Barani, D. Pizzocri, J.D. Hales, K.A. Terrani, and G. Pastore, "An investigation of FeCrAl cladding behavior under normal operating and loss of coolant conditions," *Journal of Nuclear Materials*, vol. 491, 2017, pp. 55–66.

[4] B.A. Pint, K.A. Terrani, Y. Yamamoto, and L.L. Snead, "Material selection for accident tolerant fuel cladding," *Metallurgical and Materials Transactions E*, vol. 2, 2015, pp. 190–196.

[5] K.A. Terrani, S.J. Zinkle, and L.L. Snead, "Advanced oxidation-resistant iron-based alloys for LWR fuel cladding," *Journal of Nuclear Materials*, vol. 448, 2014, pp. 420–435.

[6] S.J. Zinkle, K.A. Terrani, J.C. Gehin, L.J. Ott, and L.L. Snead, "Accident tolerant fuels for LWRs: A perspective," *Journal of Nuclear Materials*, vol. 448, 2014, pp. 374–379.

[7] J.T. Busby, "Economic benefits of advanced materials in nuclear power systems," *Journal of Nuclear Materials*, vol. 392, 2009, pp. 301–306.

[8] J. Lim, I.S. Hwang, and J.H. Kim, "Design of alumina forming FeCrAl steels for lead or lead–bismuth cooled fast reactors," *Journal of Nuclear Materials*, vol. 441, 2013, pp. 650–660.

[9] J. Lim, H.O. Nam, I.S. Hwang, and J.H. Kim, "A study of early corrosion behaviors of FeCrAl alloys in liquid lead–bismuth eutectic environments," *Journal of Nuclear Materials*, vol. 407, 2010, pp. 205–210.

[10] J. Engkvist, U. Bexell, M. Grehk, and M. Olsson, "High temperature oxidation of FeCrAl-alloys–influence of Al-concentration on oxide layer characteristics," *Materials and corrosion*, vol. 60, 2009, pp. 876–881.

[11] B.A. Pint, K.A. Unocic, and K.A. Terrani, "Effect of steam on high temperature oxidation behaviour of alumina-forming alloys," *Materials at High Temperatures*, vol. 32, 2015, pp. 28–35.

[12] R. Kögler, W. Anwand, A. Richter, M. Butterling, X. Ou, A. Wagner, and C.-L. Chen, "Nanocavity formation and hardness increase by dual ion beam irradiation of oxide dispersion strengthened FeCrAl alloy," *Journal of Nuclear Materials*, vol. 427, 2012, pp. 133–139.

[13] E. Little and D. Stow, "Void-swelling in irons and ferritic steels: II. An experimental survey of materials irradiated in a fast reactor," *Journal of Nuclear Materials*, vol. 87, 1979, pp. 25–39.

[14] K.G. Field, M.N. Gussev, Y. Yamamoto, and L.L. Snead, "Deformation behavior of laser welds in high temperature oxidation resistant Fe–Cr–Al alloys for fuel cladding applications," *Journal of nuclear materials*, vol. 454, 2014, pp. 352–358.

[15] M.O.H. Amuda and S. Mridha, “Comparative evaluation of grain refinement in {AISI} 430 {FSS} welds by elemental metal powder addition and cryogenic cooling,” *Materials & Design*, vol. 35, 2012, pp. 609–618.

[16] I. AghaAli, M. Farzam, M.A. Golozar, and I. Danaee, “The effect of repeated repair welding on mechanical and corrosion properties of stainless steel 316L,” *Materials & Design (1980-2015)*, vol. 54, 2014, pp. 331–341.

[17] M. Turski, M. Smith, P. Bouchard, L. Edwards, and P. Withers, “Spatially resolved materials property data from a uniaxial cross-weld tensile test,” *Journal of Pressure Vessel Technology*, vol. 131, 2009, p. 061406.

[18] M. Gussev, K. Field, and Y. Yamamoto, “Design, properties, and weldability of advanced oxidation-resistant FeCrAl alloys,” *Materials & Design*, vol. 129, 2017, pp. 227–238.

[19] Y. Yamamoto, B.A. Pint, K.A. Terrani, K.G. Field, Y. Yang, and L.L. Snead, “Development and property evaluation of nuclear grade wrought FeCrAl fuel cladding for light water reactors,” *Journal of Nuclear Materials*, vol. 467, 2015, pp. 703–716.

[20] J. Regina, J. Dupont, and A. Marder, “The effect of chromium on the weldability and microstructure of Fe-Cr-Al weld cladding,” *WELDING JOURNAL-NEW YORK-*, vol. 86, 2007, p. 170.

[21] S. Kobayashi and T. Takasugi, “Mapping of 475 C embrittlement in ferritic Fe–Cr–Al alloys,” *Scripta Materialia*, vol. 63, 2010, pp. 1104–1107.

[22] S.A. Briggs, P.D. Edmondson, K.C. Littrell, Y. Yamamoto, R.H. Howard, C.R. Daily, K.A. Terrani, K. Sridharan, and K.G. Field, “A combined APT and SANS investigation of α′ phase precipitation in neutron-irradiated model FeCrAl alloys,” *Acta Materialia*, vol. 129, 2017, pp. 217–228.

[23] P.D. Edmondson, S.A. Briggs, Y. Yamamoto, R.H. Howard, K. Sridharan, K.A. Terrani, and K.G. Field, “Irradiation-enhanced α′ precipitation in model FeCrAl alloys,” *Scripta Materialia*, vol. 116, 2016, pp. 112–116.

[24] M. Courtnall and F.B. Pickering, “The effect of alloying on 485 C embrittlement,” *Metal Science*, vol. 10, 1976, pp. 273–276.

[25] J. Ejenstam, M. Thuvander, P. Olsson, F. Rave, and P. Szakalos, “Microstructural stability of Fe–Cr–Al alloys at 450–550° C,” *Journal of Nuclear Materials*, vol. 457, 2015, pp. 291–297.

[26] T. Matsunaga, H. Hongo, M. Tabuchi, and R. Sahara, “Suppression of grain refinement in heat-affected zone of 9Cr–3W–3Co–VNb steels,” *Materials Science and Engineering: A*, vol. 655, 2016, pp. 168–174.

[27] B. Pint, “Experimental observations in support of the dynamic-segregation theory to explain the reactive-element effect,” *Oxidation of metals*, vol. 45, 1996, pp. 1–37.

[28] M.N. Gussev, R.H. Howard, K.A. Terrani, and K.G. Field, “Sub-size tensile specimen design for in-reactor irradiation and post-irradiation testing,” *Nuclear Engineering and Design*, vol. 320, 2017, pp. 298–308.

[29] C.M. Parish, A.P.K.K. Nimishakavi, L.L. Snead, P.D. Edmondson, K.G. Field, C.M. Silva, A.M. Williams, K.D. Linton, and K.J. Leonard, *LAMDA: irradiated-materials microscopy at Oak Ridge National Laboratory*, Oak Ridge National Laboratory (ORNL), Oak Ridge, TN (United States). Center for Nanophase Materials Sciences (CNMS), 2015.

[30] A.A. Campbell, W.D. Porter, Y. Katoh, and L.L. Snead, “Method for analyzing passive silicon carbide thermometry with a continuous dilatometer to determine irradiation temperature,” *Nuclear Instruments and Methods in Physics Research Section B: Beam Interactions with Materials and Atoms*, vol. 370, 2016, pp. 49–58.

[31] K.G. Field, M.N. Gussev, and R. Howard, “First Annual Progress Report on Radiation Tolerance of Controlled Fusion Welds in High Temperature Oxidation Resistant FeCrAl Alloys,” *ORNL/TM-2015/770.*, 2015.

[32] M.A. Sutton, J.J. Orteu, and H. Schreier, *Image correlation for shape, motion and deformation measurements: basic concepts, theory and applications*, Springer Science & Business Media, 2009.

[33] B. Cazalis, J. Desquines, S. Carassou, T.L. Jolu, and C. Bernaudat, “The plane strain tests in the PROMETRA program,” *Journal of Nuclear Materials*, vol. 472, 2016, pp. 127–142.

[34] Y.B. Das, A.N. Forsey, T.H. Simm, K.M. Perkins, M.E. Fitzpatrick, S. Gungor, and R.J. Moat, “In situ observation of strain and phase transformation in plastically deformed 301 austenitic stainless steel,” *Materials & Design*, vol. 112, 2016, pp. 107–116.

[35] L. Huynh, J. Rotella, and M.D. Sangid, “Fatigue behavior of {IN718} microtrusses produced via additive manufacturing,” *Materials & Design*, vol. 105, 2016, pp. 278–289.

[36] M. Kamaya, Y. Kitsunai, and M. Koshiishi, “True stress–strain curve acquisition for irradiated stainless steel including the range exceeding necking strain,” *Journal of Nuclear Materials*, vol. 465, 2015, pp. 316–325.

[37] C. Leitão, I. Galvão, R. Leal, and D. Rodrigues, “Determination of local constitutive properties of aluminium friction stir welds using digital image correlation,” *Materials & Design*, vol. 33, 2012, pp. 69–74.

[38] T. Nozawa, K. Ozawa, Y. Asakura, A. Kohyama, and H. Tanigawa, “Evaluation of damage accumulation behavior and strength anisotropy of NITE SiC/SiC composites by acoustic emission, digital image correlation and electrical resistivity monitoring,” *Journal of Nuclear Materials*, vol. 455, 2014, pp. 549–553.

[39] M.O. Acar and S. Gungor, “Experimental and numerical study of strength mismatch in cross-weld tensile testing,” *The Journal of Strain Analysis for Engineering Design*, 2015, p. 0309324715593699.

[40] X.G. Wang, L. Wang, and M.X. Huang, “Kinematic and thermal characteristics of Lüders and Portevin-Le Châtelier bands in a medium Mn transformation-induced plasticity steel,” *Acta Materialia*, vol. 124, 2017, pp. 17–29.

[41] M. Rossi, G. Broggiato, and S. Papalini, “Application of digital image correlation to the study of planar anisotropy of sheet metals at large strains,” *Meccanica*, vol. 43, 2008, pp. 185–199.

[42] Y. Wang and K. Murty, “Effect of temperature on mechanical anisotropy of zircaloy-4 sheet,” *Metals and Materials*, vol. 4, 1998, pp. 723–726.

[43] S. Patra, A. Ghosh, J. Sood, L.K. Singhal, A.S. Podder, and D. Chakrabarti, “Effect of coarse grain band on the ridging severity of 409L ferritic stainless steel,” *Materials & Design*, vol. 106, 2016, pp. 336–348.

[44] S. Dziaszyk, E.J. Payton, F. Friedel, V. Marx, and G. Eggeler, “On the characterization of recrystallized fraction using electron backscatter diffraction: A direct comparison to local hardness in an {IF} steel using nanoindentation,” *Materials Science and Engineering: A*, vol. 527, 2010, pp. 7854–7864.

[45] K.G. Field, S.A. Briggs, X. Hu, Y. Yamamoto, R.H. Howard, and K. Sridharan, “Heterogeneous dislocation loop formation near grain boundaries in a neutron-irradiated commercial FeCrAl alloy,” *Journal of Nuclear Materials*, vol. 483, 2017, pp. 54–61.

[46] C. Capdevila, M.K. Miller, G. Pimentel, and J. Chao, “Influence of recrystallization on phase separation kinetics of oxide dispersion strengthened Fe–Cr–Al alloy,” *Scripta Materialia*, vol. 66, 2012, pp. 254–257.

[47] K.G. Field, X. Hu, K.C. Littrell, Y. Yamamoto, and L.L. Snead, “Radiation tolerance of neutron-irradiated model Fe–Cr–Al alloys,” *Journal of Nuclear Materials,* vol. 465, 2015, pp. 746–755.

[48] A. Hishinuma, A. Kohyama, R. Klueh, D. Gelles, W. Dietz, and K. Ehrlich, “Current status and future R&D for reduced-activation ferritic/martensitic steels,” *Journal of nuclear materials*, vol. 258, 1998, pp. 193–204.

[49] X. Xie, J. Li, B. Zhang, B. Sia, and L. Yang, “Direct Measurement of R Value for Aluminum Alloy Sheet Metal Using Digital Image Correlation,” *International Digital Imaging Correlation Society*, Springer, 2017, pp. 89–94.

[50] M. Gussev, T. Byun, and J. Busby, “Description of strain hardening behavior in neutron-irradiated fcc metals,” *Journal of Nuclear Materials*, vol. 427, 2012, pp. 62–68.

[51] A. Patra and D.L. McDowell, “Crystal plasticity investigation of the microstructural factors influencing dislocation channeling in a model irradiated bcc material,” *Acta Materialia*, vol. 110, 2016, pp. 364–376.

[52] X. Wang, S. Mao, P. Chen, Y. Liu, J. Ning, H. Li, K. Zang, Z. Zhang, and X. Han, “Evolution of microstructure and mechanical properties of a dissimilar aluminium alloy weldment,” *Materials & Design*, vol. 90, 2016, pp. 230–237.